Journal of Colloid and Interface Science 469 (2016) 47–56

Contents lists available at ScienceDirect

Journal of Colloid and Interface Science

journal homepage: www.elsevier.com/locate/jcis

Surfactant-free hydrothermal synthesis of hierarchically structured spherical $CuBi_2O_4$ as negative electrodes for Li-ion hybrid capacitors

Subramanian Yuvaraj [a], Kaliyappan Karthikeyan [b], Dharmalingam Kalpana [c], Yun Sung Lee [d,*], Ramakrishnan Kalai Selvan [a,*]

[a] Solid State Ionics and Energy Devices Laboratory, Department of Physics, Bharathiar University, Coimbatore 641 046, Tamil Nadu, India
[b] Department of Mechanical and Materials Engineering, University of Western Ontario, London, Ontario N6A 5B9, Canada
[c] Central Electrochemical Research Institute – Madras Unit, Taramani, Chennai 600 113, Tamil Nadu, India
[d] Faculty of Applied Chemical Engineering, Chonnam National University, Gwangju 500-757, Republic of Korea

GRAPHICAL ABSTRACT

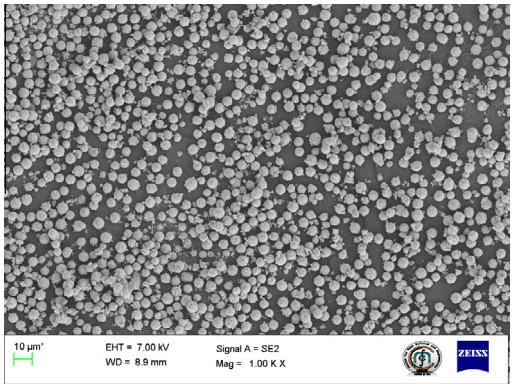

ARTICLE INFO

Article history:
Received 1 November 2015
Revised 22 January 2016
Accepted 26 January 2016
Available online 27 January 2016

Keywords:
Li-ion hybrid capacitor
Hydrothermal synthesis
Growth mechanism
$CuBi_2O_4$

ABSTRACT

Hierarchically structured spherical $CuBi_2O_4$ particles were prepared using a facile hydrothermal method without using a surfactant over various hydrothermal reaction periods. The prepared $CuBi_2O_4$ samples were examined via X-ray diffraction (XRD), which confirmed the formation of a tetragonal crystal structure. The morphological features were analyzed using field emission scanning electron microscopy (FESEM), which elucidated the construction of the hierarchical microspherical $CuBi_2O_4$ particles. The plausible growth mechanism of the hierarchical structure was explained in terms of a time-dependent synthesis process and its crystal structure. The uniform hierarchical $CuBi_2O_4$ microspheres were used to fabricate a Li-ion hybrid capacitor (Li-HC) along with activated carbon (AC), the generated device delivers a stable specific capacitance of 26.5 F g^{-1} over 1500 cycles at a high current density of 1000 mA g^{-1} and a capacity retention of ~86%. The AC/CB2 Li-ion hybrid cell exhibits high energy density and power density values of 24 W h kg^{-1} and 300 W kg^{-1}, respectively.

* Corresponding authors.
E-mail addresses: leeys@chonnam.ac.kr (Y.S. Lee), selvankram@buc.edu.in (R.K. Selvan).

http://dx.doi.org/10.1016/j.jcis.2016.01.060
0021-9797/

1. Introduction

In recent years, the utilization of nanomaterials with mesoporous hierarchical structures has been widely investigated for many applications, such as photocatalysts, sensors, supercapacitors, and Li-ion batteries [1–4]. Because these materials frequently exhibit unique properties, such as high surface area, low density, high loading capacity, more abundant active sites, and short diffusion paths for ions, they can be used to improve the fast charging and discharging process, even at high current densities [3]. Generally, nanoparticles have high surface energy, which favors self-aggregation. This behavior reduces the contact between the electrode and the electrolyte, thereby causing low capacity. Additionally, enormous volume expansion occurs in nanomaterials during the Li insertion/extraction process, which leads to capacity fading during subsequent cycles [4]. In contrast, hierarchical structures represent improvements over such nanoparticles, reducing the side reactions that occur at the electrode and electrolyte interfaces and enhancing the electrical properties of the electrodes [5,6]. Normally, hierarchical structures are considered secondary nanomaterials because they consist of large numbers of aggregated nanoparticle subunits.

In past decades, Li-ion hybrid capacitors (Li-HCs) have been intensively investigated in addition to supercapacitors and Li-ion batteries because their energy and power density fall between those of supercapacitors and Li-ion batteries. These excellent features could allow such capacitors to be utilized in hybrid electric vehicles (HEVs) and electric vehicles (EVs) [7]. Generally, Li-HCs include activated carbon (AC) as a positive electrode because of its high surface area, low cost, high chemical stability, and charge-storage mechanism, which involves an adsorption–desorption process at the electrode–electrolyte interface (non-Faradaic reaction) and improves the power density of the electrode material [8,9]. In contrast, the negative electrode consists of a Faradaic material (transition metal oxide), which stores the charge through oxidation–reduction reactions and an intercalation mechanism that increases its energy density compared to those of non-Faradaic materials [10]. Hence, a device with an intercalation anode and a capacitive cathode in an organic electrolyte should deliver enhanced energy and power densities compared to Li-ion batteries and supercapacitors [7]. However, the sluggish kinetics of Li-HCs reduces these materials' maximum energy utilization because of the imbalance between the power capabilities of the two electrodes (the non-Faradaic and Faradaic electrodes). Recently, many intercalation materials have been studied for application in Li-HCs, including the α-MnO_2, anatase, and rutile phase of TiO_2, $Li_2Ti_3O_7$, $LiCrTiO_4$, and $Li_4Ti_5O_{12}$ [8–13]. Aravindan et al. synthesized α-MnO_2 nanorods for Li-HCs including AC using a hydrothermal method and reported the maximum energy (~9 W h kg^{-1}) and power densities (~87 W kg^{-1}) [8]. Anatase- and rutile-phase TiO_2 used in Li-HCs showed high irreversible capacity loss in the first cycles, limiting these materials' practical applications [9,10]. Maximum energy densities of ~20 and ~23 W h kg^{-1} were obtained for $Li_2Ti_3O_7$ and $LiCrTiO_4$ negative electrodes, which are very similar to that of the commercially available $Li_4Ti_5O_{12}$ system [11,12]. Although $Li_4Ti_5O_{12}$ is considered to be a good candidate for Li-HCs because of this material's attractive properties, such as high coulombic efficiency, flat working potential (1.55 V vs. Li), and zero strain, it has poor ionic conductivity (<10^{-13} S cm^{-1}), a low diffusion coefficient (<10^{-6} cm^2 s^{-1}), and low theoretical capacity (175 mA h g^{-1}). Therefore, it exhibits power imbalance and reduces the energy densities of Li-HCs [13,14]. Therefore, a new type of negative electrode material with high specific capacity is needed to achieve high energy and power densities.

To satisfy this need, we prepared hierarchical $CuBi_2O_4$ microspheres as a novel negative electrode. In the structure of $CuBi_2O_4$, Cu ions are coordinated with O anions to form square planar units (CuO_4), which are stacked a top each other along the *c*-axis interconnected through BiO_2 chains [15,16]. The uniform hierarchical $CuBi_2O_4$ microspheres were synthesized through a facile surfactant-free hydrothermal method, and the growth mechanism of the hierarchical microspheres was elucidated via time-dependent experiments. The synthesized samples were characterized by different characterization techniques, such as X-ray diffraction (XRD), Raman spectroscopy, X-ray photoelectron spectroscopy (XPS), and field emission scanning electron microscopy (FESEM). Finally, the electrochemical properties of the uniform hierarchically structured $CuBi_2O_4$ particles were analyzed by cyclic voltammetry (CV), galvanostatic charge–discharge (GCD) tests, determination of the rate capabilities at different current densities, and electrochemical impedance spectroscopy (EIS).

2. Experimental section

2.1. Materials and methods

$CuBi_2O_4$ particles were derived from the starting precursors Cu $(CH_3COO)_2$, $Bi(NO_3)_3{\cdot}5H_2O$, and NaOH, which were purchased from Himedia Pvt. Ltd. (Mumbai). A stoichiometric amount of $Cu(CH_3COO)_2$ (1.5 mmol) was dissolved in 20 mL of deionized water, and $Bi(NO_3)_3{\cdot}5H_2O$ (3 mmol) was dissolved in 10 mmol of water with 1 mL of HNO_3. Then, the Bi nitrate solution was added dropwise into the Cu acetate solution. Subsequently, 1.44 g of NaOH was dissolved in 10 mL of distilled water and added to the above mixture. Next, the mixture was poured into a 75-mL Teflon-lined stainless autoclave and kept at 120 °C for 12 h. The autoclave was cooled to room temperature, and the obtained precipitate was centrifuged several times with distilled water and ethanol. The sample was dried at 80 °C for 12 h. Finally, a brown-colored $CuBi_2O_4$ (CB1) powder was obtained. This procedure was repeated using different reaction temperatures, including 140 °C, 160 °C, and 180 °C—and the products of these repetitions are denoted as CB2, CB3, and CB4, respectively.

2.2. Characterization

The phase purity of the samples was analyzed using XRD (an XPERT-PRO diffractometer with a Cu Kα (1.54178 Å) source). Fourier transform infrared (FT-IR) spectroscopy was performed using a Bruker Tensor 27 instrument with a wavenumber range of 400–4000 cm^{-1}. Raman analysis was conducted using a Horiba Jobin Yvon instrument with a 514-nm laser source in the range of 200–3000 cm^{-1}. The samples' oxidation states were analyzed using an AXIS ULTA-AXIS 165 X-ray Photoelectron Spectrometer. FESEM (JSM-6700F) and high-resolution transmission electron microscopy (HRTEM, JEOL JEM 2100) were used to examine the morphological features of the samples.

2.3. Electrode preparation

The electrochemical performances of the $CuBi_2O_4$ samples were determined using a CR2032 coin-type cell. The electrode material consisted of 75 wt% $CuBi_2O_4$ powder, 15 wt% carbon black as a conductive additive, and 10 wt% poly(vinylidene) fluoride binder dissolved in N-methylpyrrolidinone (NMP). The prepared slurry was coated on the Cu foil current collector using a slurry-casting method, and the coated foil was dried under vacuum at 90 °C overnight. The mass of the electrode materials is 5 mg. The desired electrode size was punched out of the slurry electrode. The coin

cells were assembled in a glove box filled with ultra-pure Ar by assembling a AC as cathode and $CuBi_2O_4$ acts as anode separated by a polypropylene separator (Celgard 2400). The electrolyte consisted of 1 M $LiPF_6$ dissolved in a mixture of ethylene carbonate (EC), dimethyl carbonate (DMC), and diethyl carbonate (DEC) (1:1:1; v/v). This procedure was followed to prepare the Li-HCs in which AC acts as cathode and $CuBi_2O_4$ with the same electrolyte as mentioned above. The charge–discharge studies were carried out from 0 to 3 V at different current rates in an Arbin BT-2000 Battery Test System at ambient temperature. The CV and EIS measurements were collected with an electrochemical analyzer (SP-150, Bio-Logic, France).

3. Results and discussion

3.1. Structural analysis

Fig. 1(a)–(d) shows the XRD patterns of hydrothermally prepared $CuBi_2O_4$ at different temperatures (120 °C, 140 °C, 160 °C, and 180 °C). The lattice parameter values were calculated using CELREF software and are given in Table 1. These results confirm the formation of $CuBi_2O_4$ tetragonal crystal structures (JCPDS File No. 72-0493) with the P4/ncc (130) space group. The lattice constant values exhibited decreasing '*a*' and increasing '*c*' as the reaction temperature increased, and as a result, the unit cell volume decreased and the lattice density of $CuBi_2O_4$ increased [17].

The FTIR spectrum of $CuBi_2O_4$ sample synthesized at 140 °C is shown in Fig. 2(a). This spectrum explains the characteristics peaks of $CuBi_2O_4$ at 522 and 648 cm^{-1}. The strong absorption band observed at 522 cm^{-1} is attributed to the stretching mode of the Bi–O bonds of the BiO_6 octahedron, and the small peak at 648 cm^{-1} is assigned to the stretching vibration of the Cu–O band [18]. The small absorption band at 1050 cm^{-1} corresponds to the in-plane bending vibration of C–H. The broad peaks at 1636 and 3436 cm^{-1} indicate the presence of water molecules and hydroxyl functional groups in the crystal structure resulting from the intercalation of water molecules during the synthesis [19]. Fig. 2(b) shows the Raman spectrum of the $CuBi_2O_4$ sample, which presents six Raman bands centered at 84, 123, 187, 257, 399, and 575 cm^{-1}. The band at 84 cm^{-1} is associated with the B_{2g} mode of the in-plane bending vibration of Bi rhombohedra. The strong band located at 123 cm^{-1} represents the A_{1g} mode and is assigned to the translational vibration of the CuO_4 plane along the *Z*-axis.

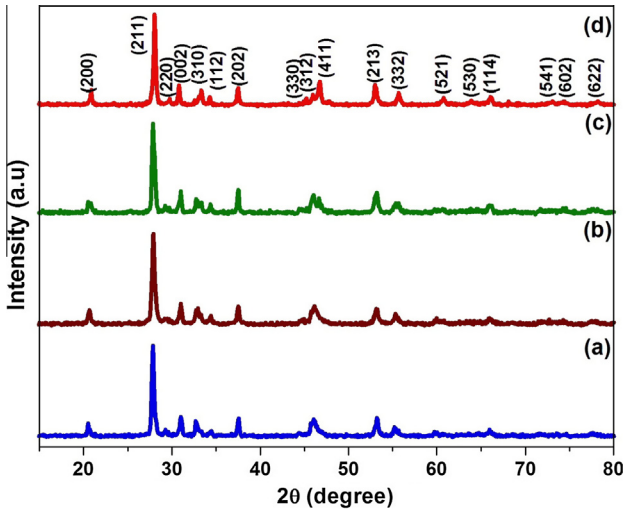

Fig. 1. (a–d) XRD patterns of $CuBi_2O_4$ synthesized at different temperatures: 120 °C, 140 °C, 160 °C, and 180 °C, respectively.

Table 1
Lattice parameter values of $CuBi_2O_4$ synthesized at different temperatures.

Hydrothermal temperature	Lattice constant (Å)		Volume (V) (Å^3)
	a	*c*	
Standard (JCPDS-72-493)	8.510	5.814	421.05
120 °C	8.614	5.784	429.29
140 °C	8.567	5.791	425.17
160 °C	8.518	5.795	420.51
180 °C	8.496	5.808	419.29

The small band at 187 cm^{-1} pertaining to the E_g mode indicates the vibration of Cu–Cu, and the highly intense band at 257 cm^{-1} corresponds to the rotation of two stacked CuO_4 squares in opposite directions [20,21]. The band observed at 399 cm^{-1} is ascribed to the A_{1g} mode of the Bi–O stretching vibration, whereas the less intense peak at 575 cm^{-1} is attributed to the A_{1g} mode of the in-plane breathing of CuO_4 squares. These values are in good agreement with those of previous reports and further confirm the tetragonal crystal structure of $CuBi_2O_4$ [20,21].

The elemental oxidation state was investigated via XPS. The survey spectrum of $CuBi_2O_4$ shown in Fig. 2(c) indicates the presence of Cu, Bi, and O. Fig. 2(d) presents the Bi 4f region. This spectrum includes two sharp and intense peaks at 159 and 164.6 eV, which correspond to the binding energies of Bi $4f_{7/2}$ and Bi $4f_{5/2}$, respectively, confirming that Bi exists in the +3 oxidation state [22]. Fig. 2(e) shows the core level of the Cu 2p spectra. The two main peaks observed at 932.2 and 952.62 eV are assigned to the binding energies of Cu $2p_{3/2}$ and Cu $2p_{1/2}$ with a spin-orbit splitting of 20.4 eV, and the two satellite peaks observed at 940.45 and 960.03 eV confirm the Cu^{2+} valence state [23]. Fig. 2(f) shows the O 2p region, which includes three deconvoluted peaks at 529.67, 531.42, and 532.89 eV. The highly intense peak located at 529.67 eV represents the O–metal bonds, and the peaks at 531.42 and 532.89 eV correspond to the adsorption of O and that of water molecules on the surfaces of the samples [24].

Fig. 3(a)–(h) shows the FESEM images of the hydrothermally prepared hierarchically structured $CuBi_2O_4$ microspheres obtained at different reaction temperatures. Fig. 3(a) and (b) presents the FESEM images of $CuBi_2O_4$ (CB1) prepared at 120 °C for 12 h and clearly reflects the evolution of uniform microspheres with outer surfaces consisting of nanocubic and spindle-shaped particles. When the hydrothermal temperature was increased to 140 °C (CB2), uniform and well-aligned hierarchical microspheres were formed, mainly from nanocubic crystals, and no spindle-like structures were detected. The microspheres continued to be produced as the temperature was further increased to 160 °C (CB3) and 180 °C (CB4). However, because of the high pressure and temperature, the characteristic morphology of the porous hierarchical structure deteriorated, and the high surface energies of the nanoparticles caused them to fuse with each other to form highly dense microsphere without pores; the outer surfaces of these microsphere have an irregular and rough appearance. The hierarchical $CuBi_2O_4$ microsphere reaction and growth mechanisms were elucidated via time-dependent experiments.

3.2. Growth mechanism of hierarchical microspheres

3.2.1. Time-dependent XRD and FESEM analyses

To identify the growth mechanism of hierarchical $CuBi_2O_4$ microspheres, the synthesis were performed using different reaction periods (1 h, 4 h, and 8 h) at the optimized reaction temperature of 140 °C, and the corresponding XRD pattern and FESEM images are shown in Figs. 4(a)–(c) and 5(a)–(e), respectively. The XRD pattern clearly indicates that all of the obtained diffraction

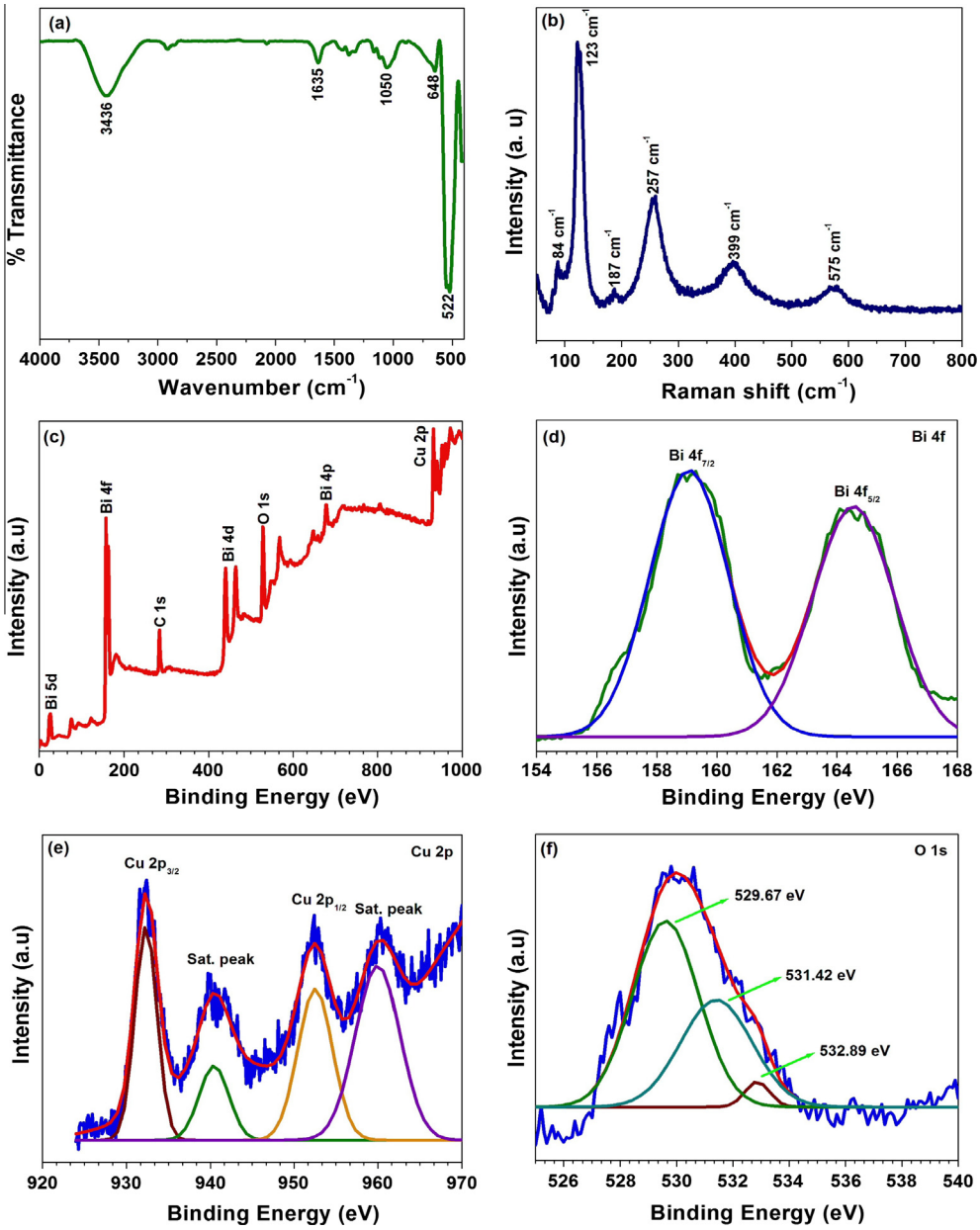

Fig. 2. (a) FTIR and (b) Raman spectra of $CuBi_2O_4$ synthesized at 140 °C for 12 h. (c) Survey spectrum of CB2 samples. (d–f) Deconvolution spectra of Bi 4f, Cu 2p, and O 1s, respectively.

peaks coincide well with the standard JCPDS file no-72-0493 and confirms the formation of $CuBi_2O_4$ with a purely tetragonal structure. The reaction mechanism of the synthesized $CuBi_2O_4$ nanoparticles is as follows [25–27],

$$Bi(NO_3)_3 + H_2O \rightarrow BiONO_3 + 2HNO_3 \quad (1)$$

$$2BiONO_3 + H_2O \rightarrow Bi_2O_2(OH)NO_3 + HNO_3 \quad (2)$$

$$Bi_2O_2(OH)NO_3 + NaOH + 2H_2O \rightarrow 2Bi(OH)_3 + NaNO_3 \quad (3)$$

$$Cu(CH_3COO)_2 + NaOH \rightarrow Cu(OH)_2 + CH_3COONa \quad (4)$$

$$2Bi(OH)_3 + Cu(OH)_2 \rightarrow CuBi_2O_4 + 4H_2O \quad (5)$$

According to the above reaction mechanism, $Bi(NO_3)_3$ reacts with water to form $Bi_2O_2(OH)NO_3$ and then further reacts with NaOH to produce $Bi(OH)_3$. Cu acetate interacts with hydroxyl ions to form $Cu(OH)_2$ precipitate. Under hydrothermal treatment, Bi $(OH)_3$ and $Cu(OH)_2$ react with each other to produce the primary $CuBi_2O_4$ nanoparticles. Fig. 5(a)–(c) shows the FESEM images of $CuBi_2O_4$ particles synthesized for 1 h. The particles appear to be non-uniform in shape, with numerous nanoparticles. At higher magnification, (Fig. 5(c)) small-sized nanorods are evident, with thicknesses of 80–150 nm and lengths of approximately 200–800 nm. Further increasing the reaction time to 4 h resulted in larger nanoparticles. Therefore, as the reaction time increases, the crystallinity of the sample increases, as confirmed by the samples XRD patterns (Fig. 4). This figure shows that both the peak intensity and the peak sharpness increase as the reaction period increases. Furthermore, when the reaction time increased to 8 h and 12 h, well-aligned hierarchical microspheres formed (Fig. 5 (f)). The morphologies of the hierarchical $CuBi_2O_4$ microspheres were determined by FESEM, and the corresponding schematic diagram is shown in Fig. 5(g).

The growth mechanism depends on a variety of factors, such as the degree of supersaturation, diffusion of the reactants, surface energy, and crystal structure in solution-based reaction systems

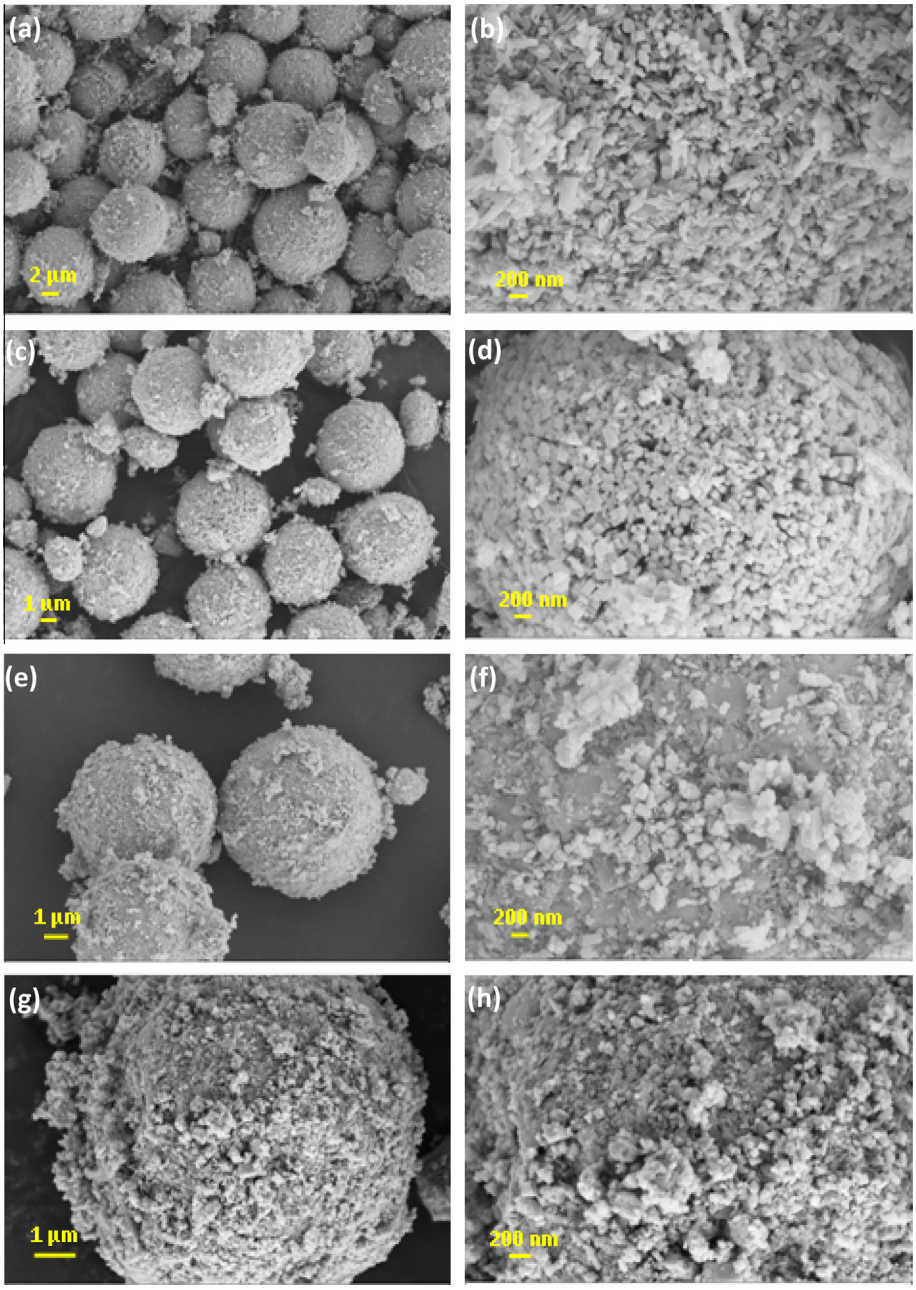

Fig. 3. High- and low-magnification FESEM images of CB1 (a, b), CB2 (b, c), CB3 (d, e), and CB4 (g, h) samples.

[28,29]. Here, the formation of microspheres occurs via three different stages: nucleation, Ostwald ripening, and self-assembly. First, nucleation begins when the precursor reacts with hydroxyl ions, leading to the formation of primary amorphous nanoparticles. Subsequently, the as-formed nanoparticles grow into larger nanorods via Ostwald ripening, i.e., larger particles are obtained at the expense of smaller ones because smaller particles are more soluble than larger ones according to the Gibbs–Thomson law [30]. This Ostwald-ripening process is further substantiated by Fig. 5 (d) and (e), in which more abundant non-uniformly shaped microspheres with large numbers of nanoparticles are observed. As the reaction time increases, the nanoparticles are suppressed, and instead, uniformly shaped microspheres are formed (Fig. 5(f)). The chemical potential and intrinsic crystal structure also influence the formation of hierarchical structures through anisotropic growth. According to the Gibbs–Thomson theory [30], the relative chemical potential of the crystal is proportional to the average dangling bonds per atom over the entire crystal [29–32]. Nanoparticles are known to have more abundant unsaturated chemical bonds or dangling bonds on their surfaces than bulk particles because of their high surface-to-volume ratio. Therefore, anisotropic growth can occur at any of the favorable crystal facets with relatively high chemical potentials, and as a result, nanoparticles tend to grow in particular orientations. The intrinsic crystal structure of $CuBi_2O_4$ consists of a tetragonal crystal structure with isolated CuO_4 square planar units of Cu^{2+} ions, which are stacked a top one another along the *c*-axis, and Bi atoms tetrahedrally coordinated by four O atoms, which are connected by a common edge to form $(BiO_2)_n$ chains along the *c*-axis [20]. Thus, in this structure, the CuO_4 squares and $(BiO_2)_n$ chains exist along the *c*-axis, and the (002) facet has more dangling bonds, imbuing the *c*-axis with a relatively high chemical potential. Therefore, based on the Gibbs–Thomson

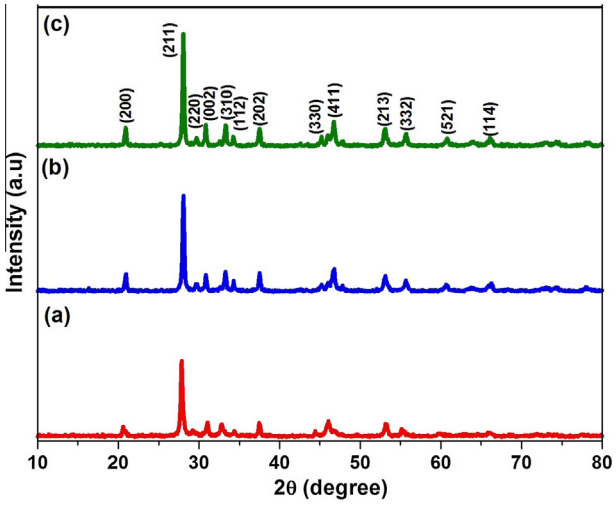

Fig. 4. (a–c) $CuBi_2O_4$ synthesized using different reaction times (1, 4, and 8 h) at 140 °C.

theory, the *c*-axis has higher chemical potential than the *a*- and *b*-axes. This result thus confirms that the *c*-axis is a more favorable direction for faster crystal growth than the other two directions. Finally, the formed nanorods were radially aligned to form uniform hierarchical microspheres through self-assembly. Similar intrinsic crystal growth phenomena has been observed in some metal tungstate and molybdate compounds [28–32]. The self-assembly process depends on both the surface energy of the system and also the relevant van der Waals forces, hydrophobic interactions, and electrostatic and dipolar fields [33]. Therefore, the formation of hierarchical microspheres mainly relies on the chemical potentials of the facets, the intrinsic crystal structure, and the Ostwald ripening process. Finally, uniform microspheres are obtained through self-assembly.

Fig. 6(a) presents the TEM images of the uniform hierarchical microspheres in the CB2 sample, which have sizes of 4–5 μm. The highly intense ultrasonication process deteriorated the microspheres, which split into small nanorods, as shown in the inset of Fig. 6(b), indicating that these microspheres mainly consist of nanorod subunits. Fig. 6(c) consists of the HRTEM images showing clear lattice fringes; their spacing (0.16 nm) corresponds to the (332) lattice plane of the tetragonal structure of $CuBi_2O_4$. The selected area electron diffraction (SAED) pattern shown in Fig. 6(d) exhibits a dot pattern, which confirms the crystalline nature of the sample, and the measured d-spacing values were 0.3384, 0.2896, 0.2605, 0.2065, 0.1849, 0.1644, and 0.1311 Å, which correspond to the lattice planes of (211), (002), (310), (330), (213), (332), and (541), respectively; these results are in good agreement with the XRD results.

3.3. Li-HCs

The electrochemical reaction mechanisms of fabricated Li-HCs were analyzed via CV in the potential window of 0–3 V at different scan rates (2–100 mV s^{-1}) in a non-aqueous electrolyte; the results are shown in Fig. 7(a). The CV curve indicates two different energy-storage mechanisms: redox (Faradaic) and EDLC (non-Faradaic) capacitive behaviors [34]. The CV curve deviates from the ideal rectangular shape when compared with the EDLC system, that elucidate the combined effect of pseudocapacitive mechanism from $CuBi_2O_4$ electrode and EDLC behavior from AC electrode. In AC/CB2 Li-ion hybrid cell, during the charging process PF_6^- anions adsorbed on the AC cathode through electric double layer mechanism (non-Faradaic process) and lithium ions are intercalated into the CB2 anode through Faradaic process, where the bismuth cation in the $CuBi_2O_4$ crystal structure change their valence state by means of oxidation reaction. On discharging process, lithium ions are liberated from the CB2 anode and PF_6^- anions desorbed from the AC cathode to attain the charge neutrality in the electrolyte solution. The charging–discharging mechanism of AC/CB2 is given as [34–36],

$$AC + xPF_6^- \leftrightarrow xPF_6^- || AC \quad (1)$$

$$CuBi_2O_4 + xLi^+ + xe^- \leftrightarrow Li_xCuBi_2O_4 \quad (2)$$

The specific capacitance of the hybrid cell was calculated using the following equation [37],

$$C = \frac{\int i\Delta t}{\Delta t \times m} = \frac{q}{\Delta V \times m}$$

where *C* is the capacitance (F g^{-1}), ΔV is the voltage change, *m* is the mass of the active materials of both electrodes, and *q* is the total voltammetric charge obtained by integrating the positive and negative sweeps. The calculated specific capacitance values are 36, 23, 22, 17, and 17 F g^{-1} for scan rates of 2, 10, 25, 50, and 100 mV s^{-1}, respectively. As shown in Fig. 7(b), the capacitance decreases as the scan rate increases. At lower scan rates, the Li ions are fully utilized by the active material's surfaces (inner and outer). However, increasing the scan rate restricts the penetration of the Li ions into the active material. Therefore, only the outer surface is involved in the Li ion intercalation process, thereby reducing the specific capacitance of the hybrid cell [8,38].

The charge–discharge studies of the AC/CB2 Li-ion hybrid cell were performed from 0 to 3 V at a current density of 1000 mA g^{-1} and are shown in Fig. 7(c). The charge–discharge process is reflected by the variation in the linear voltage over time. A perfectly triangularly shaped curve indicates EDLC behavior, whereas deviations from the triangle shape indicate that the material can store charge via different reaction mechanism; these mechanisms can be analyzed through the discharge process. The discharge curve consists of three regions: Phases I–III. The sudden voltage drop during the initial stage (Phase I) reflects the internal resistance of the electrode (R_{ESR}). Phase II is related to the capacitive component that is associated with the charge separation between the electrode and electrolyte interface [44,48]. It is associated with the electronic and ionic charge separation at the electrode and electrolyte interfaces, which provides an additional electric double layer capacitance. Finally, Phase III is relatively lengthy because of the Faradaic reaction mechanism, which is achieved using a battery-type insertion material. The charge-storage mechanism of the Li-ion hybrid cell is thus concluded to consist of both EDLC and battery-type Li-insertion mechanisms.

Fig. 7(d) presents the cycling stability curve of the AC/CB2 hybrid cell at a current density of 1000 mA g^{-1} and exhibits weak capacity fading during the initial cycles, which may be caused by the non-equilibrium states of both electrode potentials [39]. After achieving stable electrode potential, the cell shows stable specific capacitance and delivers a discharge capacity of 26.5 F g^{-1} over 1500 cycles with a capacity retention of 85.5%. This result confirms that the hybrid Li-ion capacitor exhibits excellent cycling stability with high capacity retention, possibly because of the flexibility of the one-dimensional crystal structure of $CuBi_2O_4$ and void spaces in the hierarchical structure that can accommodate the volume changes and strain during the Li ion intercalation/de-intercalation process [40].

Fig. 8(a) shows the rate performances of the AC/CB2 hybrid cell at different current densities from 50 to 1000 mA g^{-1}. The hybrid cell delivered discharge capacities of 62, 60, 59, 58, and 33 F g^{-1} at current densities of 50, 75, 200, 400, and 1000 mA g^{-1}, respectively, which indicating that the capacitance degrades as

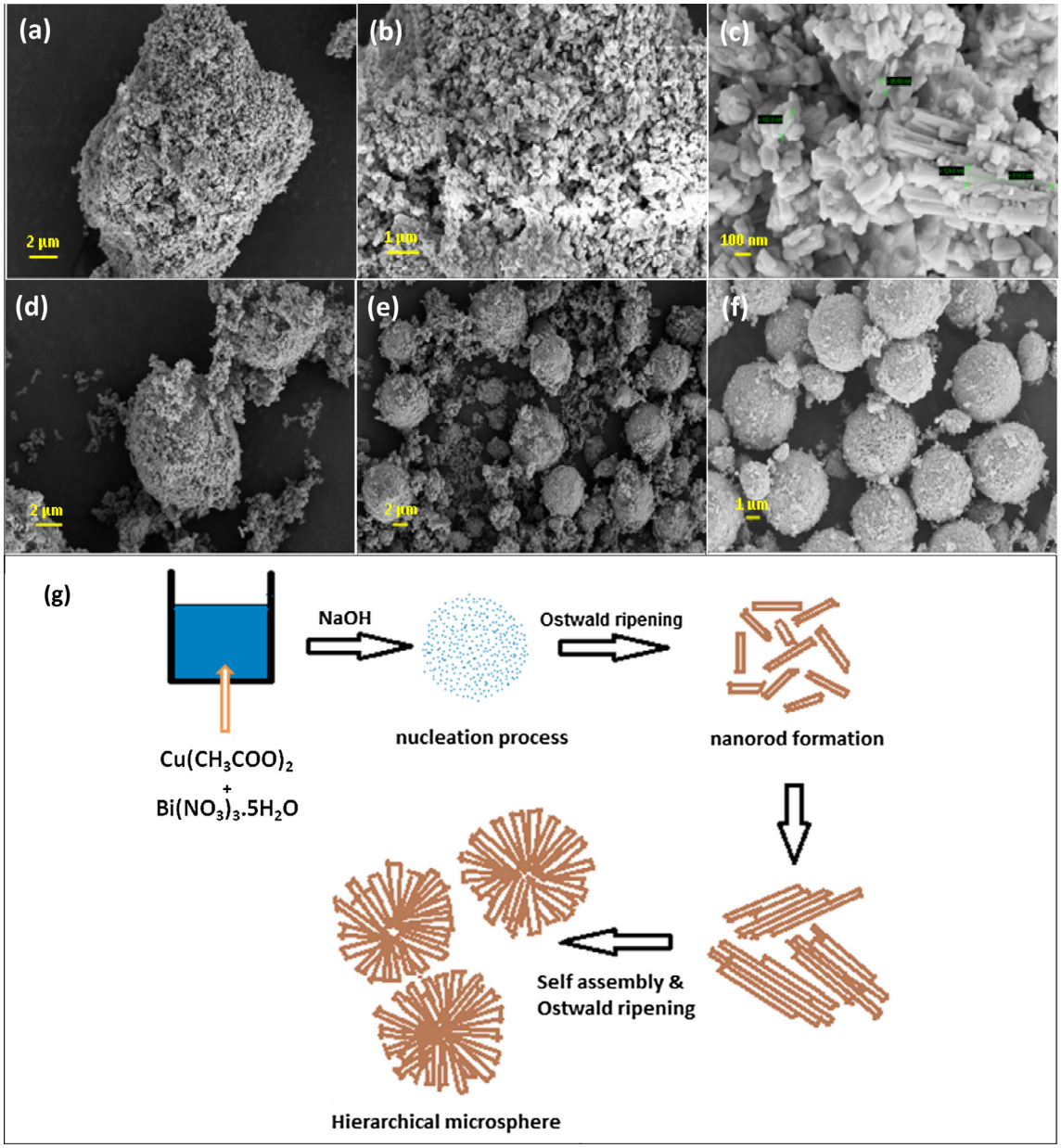

Fig. 5. (a–c) FESEM images of $CuBi_2O_4$ synthesized at 140 °C using different reaction periods: 1 h (a–c), 4 h (d), 8 h (e), and 12 h (f). The schematic diagram of the $CuBi_2O_4$ growth mechanism (g).

the current rate increases. At high current densities, Li ions do not have sufficient time to intercalate into the $CuBi_2O_4$ lattice, and thus, only the outer surface contributes to the Li ion storage mechanism. Additionally, the ionic motion at the electrode/electrolyte interface is too slow for the charge distribution to reach equilibrium at high current densities, reducing the reversible capacity of the hybrid cell [41–43]. Fig. 8(b) shows the Ragone plot that describes the relationship between the specific energy and power density of the hybrid cell, which was calculated from the galvanostatic charge–discharge curve as follows [14,34,38,44],

$$S_{PD} = \frac{IV}{2m}$$

$$S_{ED} = S_{PD} \times \frac{t}{3600}$$

where I is the applied current, V is the cell voltage, t is the discharge time, and m is the total mass of the active material in both electrodes. The hybrid cell delivers a high energy density and power density of 24 W h kg^{-1} and 300 W kg^{-1}, respectively, at the high current rate of 1000 A g^{-1}. These energies are higher than those of Bucky paper/V_2O_5 (18 W h kg^{-1}) [34], CNT/CNT (6.1 W h kg^{-1}) [36], CNT/TNW (TiO_2 nanowires) (12.5 W h kg^{-1}) [36], AC/C-$LiTi_2(PO_4)_3$ (14 W h kg^{-1}) [38], AC/α-MnO_2 (9 W h kg^{-1}) [8], AC/$Li_4Ti_5O_{12}$-C (20 W h kg^{-1}) [14], AC/TiP_2O_7 (13 W h kg^{-1}) [45], MWCNT/TiO_2-B nanowires (12.5 W h kg^{-1}) [46], and AC/L-CoS_2 (15 W h kg^{-1}) [47]; the corresponding Ragone plot is shown in Fig. 8(c).

The excellent electrochemical performance of the AC/CB2 Li-HC electrode can be explained as follows. The $CuBi_2O_4$ active material consists of numerous nanoparticles, which are held together to form the uniform hierarchical microspheres that favor Li ion and electron transport. Furthermore, their hollow interiors provide additional active sites at the electrode/electrolyte interface, imbuing the Li-HCs with good rate capability and specific capacity.

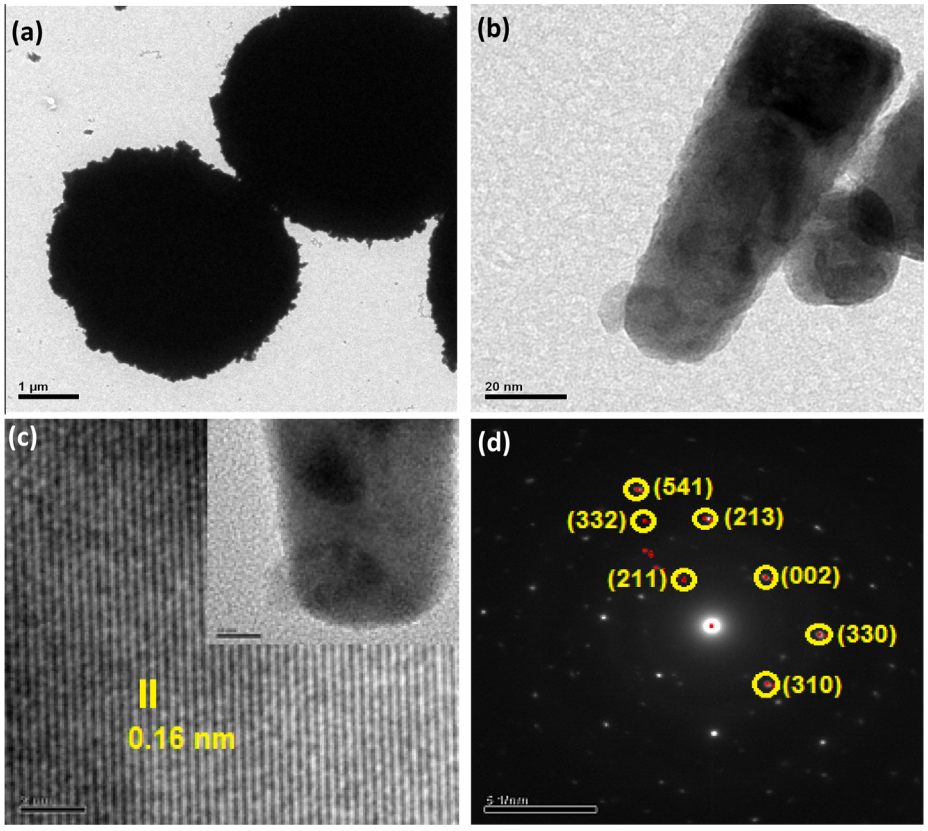

Fig. 6. (a and b) TEM image of the CB2 sample. (c and d) HRTEM image and SAED pattern of the CB2 sample respectively.

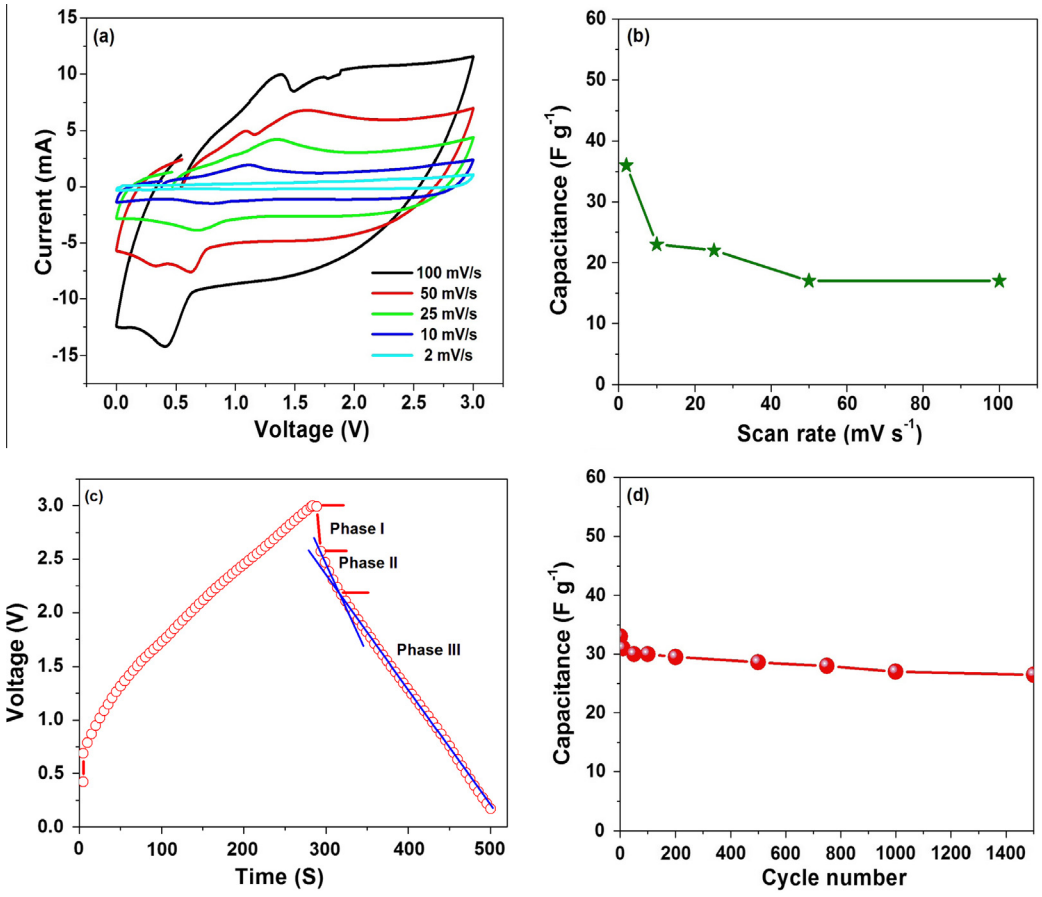

Fig. 7. (a) CV curve, (b) capacitances at different scan rates, (c) charge–discharge curve, and (d) cycling stability of the AC/CB2 Li-ion hybrid cell at 1000 mA g^{-1}.

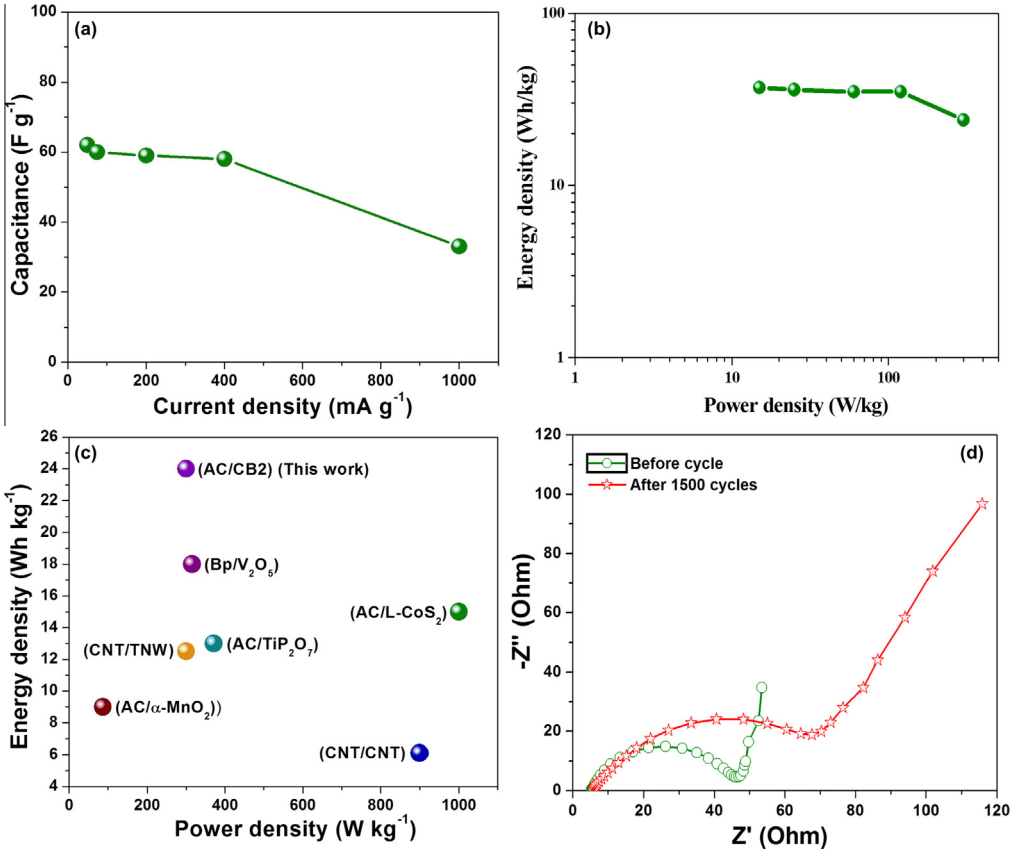

Fig. 8. (a) Rate capability curve, (b) Ragone plot of the Li-ion hybrid cell, (c) Ragone plot showing the performances of various anode materials, and (d) EIS spectra of AC/CB2 before and after cycling.

The interconnected nanoparticles facilitate the inclusion of void space within the microspheres, which can effectively accommodate the volume strain during the charging–discharging process and thus improve the cycling stability of the electrode material [5,40].

Fig. 8(d) shows the EIS spectra obtained before and after cycling the Li-ion hybrid cell in the frequency range of 100 kHz to 100 mHz at open circuit voltage. The Nyquist plot consists of two regions: the semicircle at high frequencies and the inclined line at low frequencies. The semicircle indicates the reaction kinetics at the electrode–electrolyte interface, which is known as the charge–transfer resistance (R_{ct}), and the inclined line represents the diffusion process of the Li ions within the electrode material. The EIS spectra indicates R_{ct} values of 46 and 78 Ω before and after 1500 cycles, respectively. After 1500 cycles, the charge–transfer resistance was increased because of the modification of the electrode surface resulting from the expansion and contraction that occur during the charging–discharging process [33]. The cycling stability curve also supports the EIS results, showing capacity loss during the first few cycles followed by good structural stability because of the modification of the electrode material.

4. Conclusion

The uniform hierarchical $CuBi_2O_4$ microspheres were successfully prepared using a hydrothermal method at an optimized temperature of 140 °C for 12 h. The XRD result confirms the formation of $CuBi_2O_4$ with a purely tetragonal crystal structure. The growth mechanism of the hierarchical microspheres was explained via time-dependent experimental studies and FESEM. The formation of the hierarchical structure mainly depends on the Ostwald ripening process, chemical potential, intrinsic crystal structure, and self-assembly. The Li-HCs were fabricated by combining the hierarchical $CuBi_2O_4$ microspheres with AC and exhibit a high discharge capacitance of 26.5 F g^{-1} with good cycling stability over 1500 cycles at a current density of 1000 mA g^{-1}. This behavior may be attributable to the porous structure of $CuBi_2O_4$, which allows more active sites for electrolyte interaction and accommodates the volume strain that occurs during the charging–discharging process. The AC/CB2 Li-ion hybrid cell delivers a high energy and power density of 24 W h kg^{-1} and 300 W kg^{-1}, respectively. It also exhibits excellent cycling stability, high rate capability, and high energy and power density. Therefore, it is considered to be a good electrochemical energy-storage device.

Acknowledgements

One of the authors (RKS) is grateful to UGC (No. 41-838/2012 (SR)) for their financial support under UGC-MRP. S. Yuvaraj would like to thank the UGC-BSR (No. G2/5357/2013) programme for providing the fellowship that allowed this work to be performed successfully.

References

[1] G. Tan, L. Zhang, H. Ren, S. Wei, J. Huang, A. Xia, Effects of pH on the hierarchical structures and photocatalytic performance of $BiVO_4$ powders prepared via the microwave hydrothermal method, ACS Appl. Mater. Interfaces 5 (2013) 5186–5193.

[2] X. Liu, J. Zhang, L. Wang, T. Yang, X. Guo, S. Wu, S. Wang, 3D hierarchically porous ZnO structures and their functionalization by Au nanoparticles for gas sensors, J. Mater. Chem. 21 (2011) 349–356.

[3] J.P. Cheng, X. Chen, J.S. Wu, F. Liu, X.B. Zhang, V.P. Dravid, Porous cobalt oxides with tunable hierarchical morphologies for supercapacitor electrodes, CrystEngComm 14 (2012) 6702–6709.
[4] L. Hu, H. Zhang, Y. Huang, P. Zhang, Q. Chen, $CoMn_2O_4$ spinel hierarchical microspheres assembled with porous nanosheets as stable anodes for lithium-ion batteries, Sci. Rep. 2 (986) (2011) 1–8.
[5] J. Li, S. Xiong, Y. Liu, Z. Ju, Y. Qian, High electrochemical performance of monodisperse $NiCo_2O_4$ mesoporous microspheres as an anode material for Li-ion batteries, ACS Appl. Mater. Interfaces 5 (2013) 981–988.
[6] P.G. Bruce, B. Scrosati, J.M. Tarascon, Nanomaterials for rechargeable lithium batteries, Angew. Chem. Int. Ed. 47 (2008) 2930–2946.
[7] V. Aravindan, J. Gnanaraj, Y.S. Lee, S. Madhavi, Insertion-type electrodes for nonaqueous Li-ion capacitors, Chem. Rev. 114 (2014) 11619–11635.
[8] V. Aravindan, M. Reddy, S. Madhavi, G. Rao, B. Chowdari, Electrochemical performance of α-MnO_2 nanorods/activated carbon hybrid supercapacitor, Nanosci. Nanotechnol. Lett. 4 (2012) 724–728.
[9] Y. Cai, B. Zhao, J. Wang, Z. Shao, Non-aqueous hybrid supercapacitors fabricated with mesoporous TiO_2 microspheres and activated carbon electrodes with superior performance, J. Power Sources 253 (2014) 80–89.
[10] J.-Y. Shin, D. Samuelis, J. Maier, Sustained lithium-storage performance of hierarchical, nanoporous anatase TiO_2 at high rates: emphasis on interfacial storage phenomena, Adv. Funct. Mater. 21 (2011) 3464–3472.
[11] W. Cho, M.-S. Park, J.-H. Kim, J.-H. Kim, Interfacial reaction between electrode and electrolyte for a ramsdellite type $Li_{2+x}Ti_3O_7$ anode material during lithium insertion, J. Electrochim. Acta 63 (2012) 263–268.
[12] V. Aravindan, W. Chuiling, S. Madhavi, High power lithium-ion hybrid electrochemical capacitors using spinel $LiCrTiO_4$ as insertion electrode, J. Mater. Chem. 22 (2012) 16026–16031.
[13] Z. Yang, D. Choi, S. Kerisist, K.M. Rosso, D. Wang, J. Zhang, G. Graff, J. Liu, Nanostructures and lithium electrochemical reactivity of lithium titanites and titanium oxides: a review, J. Power Sources 192 (2009) 588–598.
[14] J. Ni, L. Yang, H. Wang, L. Gao, A high-performance hybrid supercapacitor with $Li_4Ti_5O_{12}$–C nano-composite prepared by in situ and ex situ carbon modification, J. Sol. State Electrochem. 16 (2012) 2791–2796.
[15] J.P. Attfield, Exchange striction and exchange constants in Bi_2CuO_4, J. Phys.: Condens. Matter 1 (1989) 7045–7053.
[16] J.L. Garcia-Munoz, J. Rodriguez-Carvajal, F. Sapina, Crystal and magnetic structures of Bi_2CuO_4, J. Phys.: Condens. Matter 2 (1990) 2205–2214.
[17] S. Saravanakumar, R. Saravanan, S. Sasikumar, Effect of sintering temperature on the magnetic properties and charge density distribution of nano-NiO, Chem. Pap. 68 (6) (2014) 788–797.
[18] H.Y. Jiang, J. Liu, K. Cheng, W. Sun, J. Lin, Enhanced visible light photocatalysis of Bi_2O_3 upon fluorination, J. Phys. Chem. C 117 (2013) 20029–20036.
[19] J. Yu, Y. Le, B. Cheng, Fabrication and CO_2 adsorption performance of bimodal porous silica hollow spheres with amine-modified surfaces, RSC Adv. 2 (2012) 6784–6791.
[20] Z.V. Popovic, G. Kliche, M. Cardona, A. Liu, Vibrational properties of Bi_2CuO_4, Phys. Rev. B 41 (1990) 3824–3828.
[21] F.X. Zhang, S.K. Saxena, Raman studies of Bi_2CuO_4 at high pressures, Appl. Phys. Lett. 88 (2006) 141926–141929.
[22] J. Hou, Z. Wang, S. Jiao, H. Zhu, Bi_2O_3 quantum-dot decorated nitrogen-doped Bi_3NbO_7 nanosheets: in situ synthesis and enhanced visible-light photocatalytic activity, CrystEngComm 14 (2012) 5923–5928.
[23] D. Ranjith Kumar, D. Manoj, J. Santhanalakshmi, Optimization of site specific adsorption of oleylamine capped CuO nanoparticles on MWCNTs for electrochemical determination of guanosine, Sens. Actuat. B 188 (2013) 603–612.
[24] M. Huang, Y. Zhang, F. Li, Z. Wang, Alamusi, N. Hu, Z. Wen, Q. Liu, Merging of Kirkendall growth and Ostwald ripening: CuO@MnO_2 core–shell architectures for asymmetric supercapacitors, Sci. Rep. 4 (2014) 1–9 4518.
[25] A.M. Abdulkarem, J. Li, A.A. Aref, L. Ren, E.M. Elssfah, H. Wang, Y. Ge, Y. Yu, $CuBi_2O_4$ single crystal nanorods prepared by hydrothermal method: growth mechanism and optical properties, Mater. Res. Bull. 46 (2011) 1443–1450.
[26] C. Wu, L. Shen, Q. Huang, Y.C. Zhang, Hydrothermal synthesis and characterization of Bi_2O_3 nanowires, Mater. Lett. 65 (2011) 1134–1136.
[27] G.H. Du, G.V. Tendeloo, $Cu(OH)_2$ nanowires, CuO nanowires and CuO nanobelts, Chem. Phys. Lett. 393 (2004) 64–69.
[28] X.Y. Chen, C. Ma, X.X. Li, P. Chen, J.G. Fang, Hierarchical Bi_2CuO_4 microspheres: hydrothermal synthesis and catalytic performance in wet oxidation of methylene blue, Cat. Commun. 10 (2009) 1020–1024.
[29] B.S. Hong, B. Liu, M.S. Mo, J.H. Huang, X.M. Liu, Y.T. Qian, General synthesis of single-crystal tungstate nanorods/nanowires: a facile, low-temperature solution approach, Adv. Funct. Mater. 13 (2003) 639–647.
[30] J.W. Mullin, Crystallization, third ed., Butterworth-Heinemann, Oxford, UK, 1997.
[31] Y. Li, J. Liu, X. Huang, G. Li, Hydrothermal synthesis of Bi_2WO_6 uniform hierarchical microspheres, Cryst. Growth Des. 7 (2007) 1350–1355.
[32] C. Zhang, Y. Zhu, Synthesis of square Bi_2WO_6 nanoplates as high-activity visible-light-driven photocatalysts, Chem. Mater. 17 (2005) 3537–3545.
[33] S. Song, Y. Zhang, J. Feng, Y. Xing, Y. Lei, W. Fan, H. Zhang, Self-assembled growth of $AgIn(MoO_4)_2$ submicroplates into hierarchical structures and their near-infrared luminescent properties, Cryst. Growth Des. 9 (2009) 848–852.
[34] V. Aravindan, Y.L. Cheah, W.F. Mark, G. Wee, B.V.R. Chowdari, S. Madhavi, Fabrication of high energy-density hybrid supercapacitors using electrospun V_2O_5 nanofibers with a self-supported carbon nanotube network, ChemPlusChem 77 (2012) 570–575.
[35] G.G. Amatucci, F. Badway, A. Du Pasquier, T. Zheng, An asymmetric hybrid nonaqueous energy storage cell, J. Electrochem. Soc. 148 (2001) A930–A939.
[36] Q. Wang, Z.H. Wen, J.H. Li, A hybrid supercapacitor fabricated with a carbon nanotube cathode and a TiO_2–B nanowire anode, Adv. Funct. Mater. 16 (2006) 2141–2146.
[37] H. Kim, M.-Y. Cho, M.-H. Kim, K.-Y. Park, H. Gwon, Y. Lee, K.C. Roh, K.A. Kang, Novel high-energy hybrid supercapacitor with an anatase TiO_2–reduced graphene oxide anode and an activated carbon cathode, Adv. Energy Mater. 3 (2013) 1500–1506.
[38] V. Aravindan, W. Chuiling, M.V. Reddy, G.V.S. Rao, B.V.R. Chowdari, S. Madhavi, Carbon coated nano-$LiTi_2(PO_4)_3$ electrodes for non-aqueous hybrid supercapacitors, Phys. Chem. Chem. Phys. 14 (2012) 5808–5814.
[39] V. Khomenko, E. Raymundo-Pinero, F. Beguin, Optimisation of an asymmetric manganese oxide/activated carbon capacitor working at 2 V in aqueous medium, J. Power Sources 153 (2006) 183–190.
[40] Y. Feng, X. Li, Z. Shao, H. Wang, Morphology-dependent performance of Zn_2GeO_4 as a high-performance anode material for rechargeable lithium ion batteries, J. Mater. Chem. A 3 (2015) 15274–15279.
[41] K. Zaghib, J.B. Goodenough, A. Mauger, C. Julien, Unsupported claims of ultrafast charging of $LiFePO_4$ Li-ion batteries, J. Power Sources 194 (2009) 1021–1023.
[42] X.M. Wu, X.H. Li, Z. Wang, Z.B. Xiao, J. Liu, W.B. Yan, Characterization of solution-derived $LiMn_2O_4$ thin films heat-treated by rapid thermal annealing, Mater. Chem. Phys. 83 (2004) 78–81.
[43] J.B. Goodenough, Y. Kim, Challenges for rechargeable Li batteries, Chem. Mater. 22 (2010) 587–603.
[44] K. Karthikeyan, S. Amaresh, V. Aravindan, H. Kim, K.S. Kang, Y.S. Lee, Unveiling organic–inorganic hybrids as a cathode material for high performance lithium-ion capacitors, J. Mater. Chem. A 1 (2013) 707–714.
[45] V. Aravindan, M.V. Reddy, S. Madhavi, S.G. Mhaisalkar, G.V. Subba Rao, B.V.R. Chowdari, Hybrid supercapacitor with nano-TiP_2O_7 as intercalation electrode, J. Power Sources 196 (2011) 8850–8854.
[46] Q. Wang, Z.H. Wen, J.H. Li, A hybrid supercapacitor fabricated with a carbon nanotube cathode and a TiO_2–B nanowire anode, Adv. Funct. Mater. 16 (2006) 2141–2146.
[47] S. Amaresh, K. Karthikeyan, I.-C. Jang, Y.S. Lee, Single-step microwave mediated synthesis of the CoS_2 anode material for high rate hybrid supercapacitors, J. Mater. Chem. A 2 (2014) 11099–11106.
[48] K. Karthikeyan, S. Amaresh, K.J. Kim, S.H. Kim, K.Y. Chung, B.W. Cho, Y.S. Lee, A high performance hybrid capacitor with Li_2CoPO_4F cathode and activated carbon anode, Nanoscale 5 (2013) 5958.